Delays, Detours, and Forks in the Road: Latent State Models of Training Dynamics

Anonymous authors
Paper under double-blind review

Abstract

The impact of randomness on model training is poorly understood. How do differences in data order and initialization actually manifest in the model, such that some training runs outperform others or converge faster? Furthermore, how can we interpret the resulting training dynamics and the phase transitions that characterize different trajectories? To understand the effect of randomness on the dynamics and outcomes of neural network training, we train models multiple times with different random seeds and compute a variety of metrics throughout training, such as the L_2 norm, mean, and variance of the neural network's weights. We then fit a hidden Markov model (HMM; Baum & Petrie, 1966) over the resulting sequences of metrics. The HMM represents training as a stochastic process of transitions between latent states, providing an intuitive overview of significant changes during training. Using our method, we produce a low-dimensional, discrete representation of training dynamics on grokking tasks, image classification, and masked language modeling. We use the HMM representation to study phase transitions and identify latent "detour" states that slow down convergence.

1 Introduction

We possess strong intuition for how various tuned hyperparameters, such as learning rate or weight decay, affect model training dynamics and outcomes (Galanti et al., 2023; Lyu et al., 2022). For example, a larger learning rate may lead to faster convergence at the cost of sub-optimal solutions (Hazan, 2019; Smith et al., 2021; Wu et al., 2019). However, we lack similar intuitions for the impact of randomness. Like other hyperparameters, random seeds also have a significant impact on training (Madhyastha & Jain, 2019; Sellam et al., 2022), but we have a limited understanding of how randomness in training actually manifests in the model.

In this work, we study the impact of random seeds through a low-dimensional representation of training dynamics, which we use to visualize and cluster training trajectories with different parameter initializations and data orders. Specifically, we analyze training trajectories using a **hidden Markov model** (HMM) fitted on a set of generic metrics collected throughout training, such as the means and variances of the neural network's weights and biases. From the HMM, we derive a visual summary of how learning occurs for a task across different random seeds.

This work is a first step towards a principled and automated framework for understanding variation in model training. By learning a low-dimensional representation of training trajectories, we analyze training at a higher level of abstraction than directly studying model weights. We use the HMM to infer a Markov chain over latent states in training and relate the resulting paths to training outcomes.

Our contributions:

1. We propose to use the HMM as a principled, automated, and efficient method for analyzing variability in model training. We fit the HMM to a set of off-the-shelf metrics and allow the model to infer latent state transitions from the metrics. We then extract from the HMM a "training map," which describes the important metrics for each state and changes in these metrics during state transitions, helping to visualize how training evolves (Section 2).

We train HMMs on training trajectories derived from grokking tasks, language modeling, and image classification across a variety of model architectures and sizes. For these settings, we use the training map to characterize how different random seeds lead to different training trajectories. We analyze phase transitions in grokking by matching them to corresponding latent states in the training map, and thus the changes in metrics associated with the phase transitions (Section 3.1).

2. We discover **detour** states, which are latent states associated with slower convergence. We propose our method for finding detour states as a general way to assign semantics onto latent states in training maps (Sections 2.3, 3.4).

   We discover that we can induce detour states in image classification by destabilizing the optimization process and, conversely, remove detour states in grokking by stabilizing the optimization process. By making a few changes that are known to stabilize neural network training, such adding normalization layers, we find that the gap between memorization and generalization in grokking is dramatically reduced. Our results, along with prior work from Liu et al. (2023), show that grokking can be avoided by changing the architecture or optimization of deep networks (Section 3.3).

2 Methods

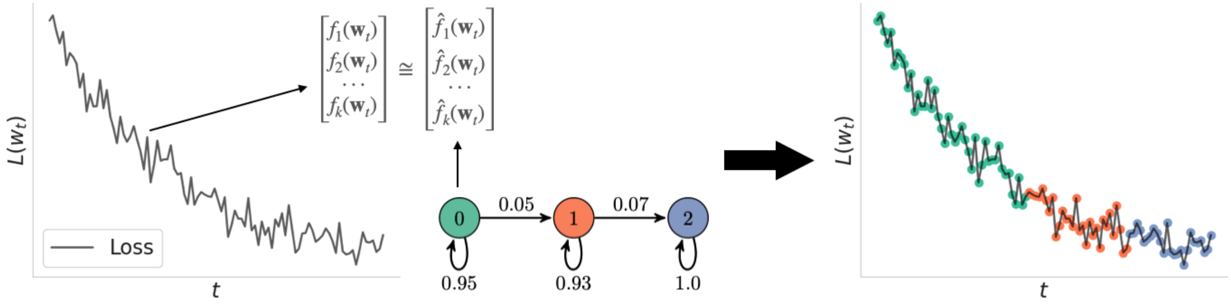
$L(w_t)$
Loss
t
$\begin{bmatrix} f_1(\mathbf{w}_t) \\ f_2(\mathbf{w}_t) \\ \cdots \\ f_k(\mathbf{w}_t) \end{bmatrix} \cong \begin{bmatrix} \hat{f}_1(\mathbf{w}_t) \\ \hat{f}_2(\mathbf{w}_t) \\ \cdots \\ \hat{f}_k(\mathbf{w}_t) \end{bmatrix}$
0
1
2
0.05
0.07
0.95
0.93
1.0
$L(w_t)$
t

Figure 1: From training runs we collect metrics, which are functions of the neural networks' weights. We then train a hidden Markov model using the sequences of metrics generated from the training runs. The hidden Markov model learns a discrete latent state over the sequence, which we use to cluster and analyze the training trajectory.

In this work, we cluster training trajectories from different random seeds and then analyze these clusters to better understand their learning dynamics and how they compare to each other. To cluster trajectories, we assign each model checkpoint to a discrete latent state using an HMM. We choose the HMM because it is the simplest time series model with a discrete latent space.

Let $\mathbf{w}_{1:T} \in \mathbb{R}^{D \times T}$ be the sequence of neural network weights observed during training. Each $\mathbf{w}_t$ is a model checkpoint. In this work, we use the Gaussian HMM to label each checkpoint $\mathbf{w}_{1:T}$ with its own latent state, $s_{1:T}$. Fitting the HMM directly over the weights is computationally infeasible, because the sample complexity of an HMM with $O(D^2)$ parameters would be prohibitively high. Our solution to this problem is to compute a small number of metrics $f_1(\mathbf{w}_{1:T}), \ldots, f_d(\mathbf{w}_{1:T})$ from $\mathbf{w}_{1:T}$, where $d << D$ and $f : \mathbb{R}^D \to \mathbb{R}$.

2.1 Training an HMM over Metrics

In this work, we focus on capturing how the computation of the neural network changes during training by modeling the evolution of the neural network weights. To succinctly represent the weights, we compute various metrics such as the average layer-wise L_1 and L_2 norm, the mean and variances of the weights and biases in the network, and the means and variances of each weight matrix's singular values. A full list of the 14 metrics we use, along with formulae and rationales, is in Appendix B.

To fit the HMM, we concatenate these metrics into an observation sequence $z_{1:T}$. We then apply z-score normalization (also known as standardization), adjusting each feature to have a mean of zero and a standard deviation of one, as HMMs are sensitive to the scale of features. We thus obtain the normalized sequence $\tilde{z}_{1:T}$. To bound the impact of training trajectory length, we compute z-scores using the estimated mean and variance of (up to) the first 1000 collected checkpoints.

$$z_t = \begin{bmatrix} f_1(\mathbf{w}_t) \\ \vdots \\ f_d(\mathbf{w}_t) \end{bmatrix}, \qquad \tilde{z}_t = \begin{bmatrix} [f_1(\mathbf{w}_t) - \mu(f_1(\mathbf{w}_{1:T}))]/\sigma(f_1(\mathbf{w}_{1:T})) \\ \vdots \\ [f_d(\mathbf{w}_t) - \mu(f_d(\mathbf{w}_{1:T}))]/\sigma(f_d(\mathbf{w}_{1:T})) \end{bmatrix}$$

We collect N sequences $\{z_{1:T}\}_1^N$ from N different random seeds, normalize the distribution of each metric across training for a given seed, and train the HMM over the sequences $\{\tilde{z}_{1:T}\}_1^N$ using the Baum-Welch algorithm (Baum et al., 1970). The main hyperparameter in the HMM is the number of hidden states, which is typically tuned using the log-likelihood, Akaike information criterion (AIC), and/or Bayesian information criterion (BIC) (Akaike, 1998; Schwarz, 1978) of validation sequences. Here, we hold out 20% of the N trajectories as validation sequences and choose the number of hidden states that minimizes the BIC. We use BIC because BIC imposes a stronger preference for simpler, and thus more interpretable, models. Model selection curves are in Appendix G.

2.2 Extracting the Training Map

Next, we use the HMM to describe what each hidden state means and how the hidden states relate to each other. We convert the HMM into a "training map," which represents hidden states as vertices in a graph and hidden state transitions as edges in the graph.

First, we extract the graph's structure from the HMM. The learned HMM has two sets of parameters: the transition matrix $p(s_t|s_{t-1})$ between hidden states, and the emission distribution $p(\tilde{z}_t|s_t = k) \sim N(\mu_k, \Sigma_k)$, where μ_k and Σ_k are the mean and covariance of the Gaussian conditioned on the hidden state k, respectively. The transition matrix is a Markov chain that defines the graph's structure. It defines what hidden states exist and the possible transitions between hidden states *a priori*. We prune edges in the Markov chain if the edge is unused by the HMM for all training trajectories.

We label the hidden states $s_{1:T}$ (i.e., the graph's vertices) by ranking the features according to how much each feature $\tilde{z}_t[i]$ changes the posterior probability $p(s_t = k|\tilde{z}_{1:t})$. If a change $\Delta\tilde{z}_t[i]$ along a feature $\tilde{z}_t[i]$ leads to a large change in $p(s_t = k|\tilde{z}_{1:t})$, then we consider $\tilde{z}_t[i]$ to be an influential feature for the prediction that $s_t = k$. Let $\mathcal{L}$ be the likelihood $p(\tilde{z}_t|s_t)$.

Proposition 1 *We can rank features $\tilde{z}_t[i]$ according to how much they change the posterior probability $p(s_t = k|\tilde{z}_{1:t})$ by computing the derivative:*

$$\frac{\partial \log \mathcal{L}}{\partial \Delta \tilde{z}_t[i]} = \Sigma_k^{-1}[i,i] \tag{1}$$

***Proof sketch**: The posterior probability $p(s_t|\tilde{z}_{1:t})$ is a monotonic transformation of the likelihood $\mathcal{L}$ when holding $\tilde{z}_{1:t-1}$ fixed. Thus, we can simply take the derivative $\frac{\partial \log \mathcal{L}}{\partial \Delta \tilde{z}_t[i]} = \Sigma_k^{-1}[i,i]$ to find the features $\tilde{z}_t[i]$ that produce the largest changes in the log-likelihood. It follows that the most important feature $\tilde{z}_t[i]$ for hidden state k has the largest $\Sigma_k^{-1}[i,i]$. See Appendix A for the full derivation.*

In the results to follow, we use Proposition 1 to compute the 3 most important features for each hidden state. Formally, the most important feature is $\arg\max_{\tilde{z}_t[i]} \frac{\partial \log \mathcal{L}}{\partial \Delta \tilde{z}_t[i]}$.

To characterize an edge $(j \to k)$ in the graph, we can subtract the means between state j and k. The difference vector $\mu_k - \mu_j$ then describes the movement of features along the edge. In summary, we can obtain a training map from an HMM by extracting:

- The graph structure (vertices and edges) from a pruned transition matrix.
- Vertex labels from the learned covariance matrix of each hidden state, which describes the features that change the hidden state the most.
- Edge labels from the difference vectors between hidden states.

2.3 Assigning Semantics to Latent States

From the HMM's transition matrix, we obtain a training map, or the Markov chain between learned latent states of training. We then label the nodes and edges in the training map using probabilistic reasoning over the HMM's learned means and covariances. But what do we learn from the path a training run takes through the map? In particular, what impact does a particular state have on training outcomes?

In order to relate HMM states to training outcomes, we select a metric and predict it from the path a training run takes through the Markov chain. To do so, we must featurize the sequence of latent states, and in this work we use unigram featurization, or a "bag of states" model. Formally, let $s_1, s_2, \ldots, s_T$ be the latent states visited during a training run. The empirical distribution over states can be calculated as:

$$\hat{P}(s = k) = \frac{\sum_j \mathbb{1}(s_j = k)}{T} \tag{2}$$

where k represents a particular state and T is the total number of checkpoints in the trajectory. This distribution can be written as a d-dimensional vector, which is equivalent to unigram featurization.

In this work, we investigate how particular states impact convergence time, which we measure as the first timestep that evaluation accuracy crosses a threshold. We set the threshold to be a value slightly smaller than the maximum evaluation accuracy (see Section 3.4). We use linear regression to predict convergence time from $\hat{P}$. Here, we are not forecasting when a model will converge from earlier timesteps; rather, we are simply using linear regression to learn a function between latent states and convergence time.

After training the regression model, we examine the regression coefficients to see which states are correlated with slower or faster convergence times. If the regression coefficient for a state is positive when predicting convergence time, then a training run spending additional time in that state implies longer convergence time. Additionally, if that same state is not visited by all trajectories, then we can consider it a **detour**, because the trajectories that visit the optional state are also delaying their convergence time.

Definition: Detour state.

A learned latent state is a detour state if:

- Some training runs converge without visiting the state. This indicates that the state is "optional."
- Its linear regression coefficient is positive when predicting convergence time. This indicates that a training run spending more time in the state will have a longer convergence time.

Our method for assigning semantics to latent states can be extended to other metrics. For example, one might use regression to predict a measure of gender bias, which can vary widely across training runs (Sellam et al., 2022), from the empirical distribution over latent states. The training map then becomes a map of how gender bias manifests across training runs. We also recommend computing the p-value of the linear regression and only interpreting the coefficients when they are statistically significant.

3 Results

Training maps help us understand how and when variations due to randomness manifest over the course of training. We perform experiments across five tasks: modular addition, sparse parities, masked language modeling, MNIST, and CIFAR-100. For all training hyperparameter details, see Appendix C.

Modular arithmetic and sparse parities are tasks where models consistently exhibit **grokking** (Power et al., 2022), a phenomenon where the training and validation losses seem to be decoupled, and the validation loss drops sharply after a period of little to no improvement. The model first memorizes the training data and then generalizes to the validation set. We call these sharp changes "phase transitions," which are periods in training which contain an inflection in the loss (i.e., the concavity of the loss changes) that is then sustained (no return to chance performance).

We study modular arithmetic and sparse parities to see how phase transitions are represented by the HMM's discrete latent space. We complement these tasks with masked language modeling (Appendix D) and image classification. In this work, we ignore embedding matrices and layer norms when computing metrics, as we are primarily interested in how the function represented by the neural network changes.

3.1 Algorithmic Data: Modular Arithmetic and Sparse Parities

Modular Arithmetic: Figure 2. In modular addition, we train a one-layer autoregressive transformer to predict $z = (x + y) \mod 113$ from inputs x and y. We collect trajectories using 40 random seeds and train and validate the HMM on a random 80-20 validation split, a split that we use for all settings. This is a replication of the experiments in Nanda et al. (2023).

In modular arithmetic, the number of epochs that different training runs take to converge differ by thousands of epochs. Examining the modular addition training map, we find that there exist paths of different lengths: some training runs take the shortest path through the map to convergence, while others do not. We feature three such paths in Figure 2. All runs initialize in state 1 and achieve low loss in state 3, but there are several paths from 1 to 3. The longest path ($1 \to 5 \to 2 \to 3$) coincides with the longest time to convergence of the three featured runs, and the shortest path ($1 \to 3$) with the shortest.

Using the HMM, we can further dissect this variability by relating the edges exiting state 1 to how fast or slow generalizing runs differ with respect to model internals. The results of this examination are in the table of Figure 2. Here, we take the top 3 features of states 2, 5, and 3 via the learned covariance matrices, and quantify the feature movements of the top 3 features by subtracting the learned means (recall $\tilde{z}$) between these states and state 1. We find that the fast-generalizing path ($1 \to 3$) is characterized by a "just-right" drop in the L_2 norm ($\downarrow$1.68, see table). The slower-generalizing runs ($1 \to 2 \to 3$) and ($1 \to 5 \to 2 \to 3$) are characterized by either smaller ($\downarrow$0.59) or larger ($\downarrow$2.08) drops in L_2 norm.

State 1 encapsulates the memorization phase transition: the training loss drop to near-zero in state 1, while validation loss increases. Thus, according to the training map, the epoch in which the generalization phase transition happens is affected by how fast the L_2 norm drops immediately after the memorization phase transition. A "just-right" drop in the L_2 norm is correlated with the quickest onset of generalization.

Sparse Parities: Figure 8 in Appendix E. Sparse parities is a similar rule-based task to modular addition, where a multilayer perceptron must learn to apply an AND operation to 3 bits within a 40-length bit vector; the crux of the task is learning which 3 of the 40 bits are relevant. We again collect 40 training runs.

Similar to modular arithmetic, path variability through the training map also appears at the beginning of training in sparse parities. Slow-generalizing runs take the path ($2 \to 0 \to 5$), while fast-generalizing runs take the more direct path ($2 \to 5$). The L_2 norm remains important here, with the edge ($2 \to 0$) characterized by an increase in the L_2 norm and the edge ($2 \to 5$) characterized by a decrease. Once again, the speed at which the generalization phase transition occurs is associated with a specific change in the L_2 norm immediately after the memorization phase transition.

3.2 Image classification: CIFAR-100 and MNIST

CIFAR-100: Figure 3 As a counterpoint to grokking, consider image classification, a well-studied task in computer vision and machine learning. We collect 40 runs of ResNet18 (He et al., 2016) trained on CIFAR-100 (Krizhevsky, 2009), and find that the learning dynamics are smooth and insensitive to random seed. The training map is a linear graph, and the state transitions all tend to feature increasing dispersion in the weights. We show the top 3 features for each state transition in the table of Figure 3. The L_1, L_2 and average singular value are increasing monotonically across all state transitions.

MNIST: Figure 9 in Appendix F. The dynamics of CIFAR-100 seem to be shared by MNIST. We collect 40 training runs of a two-layer MLP learning image classification on MNIST, with hyperparameters based on Simard et al. (2003). The training runs of MNIST follow a single trajectory through the training map.

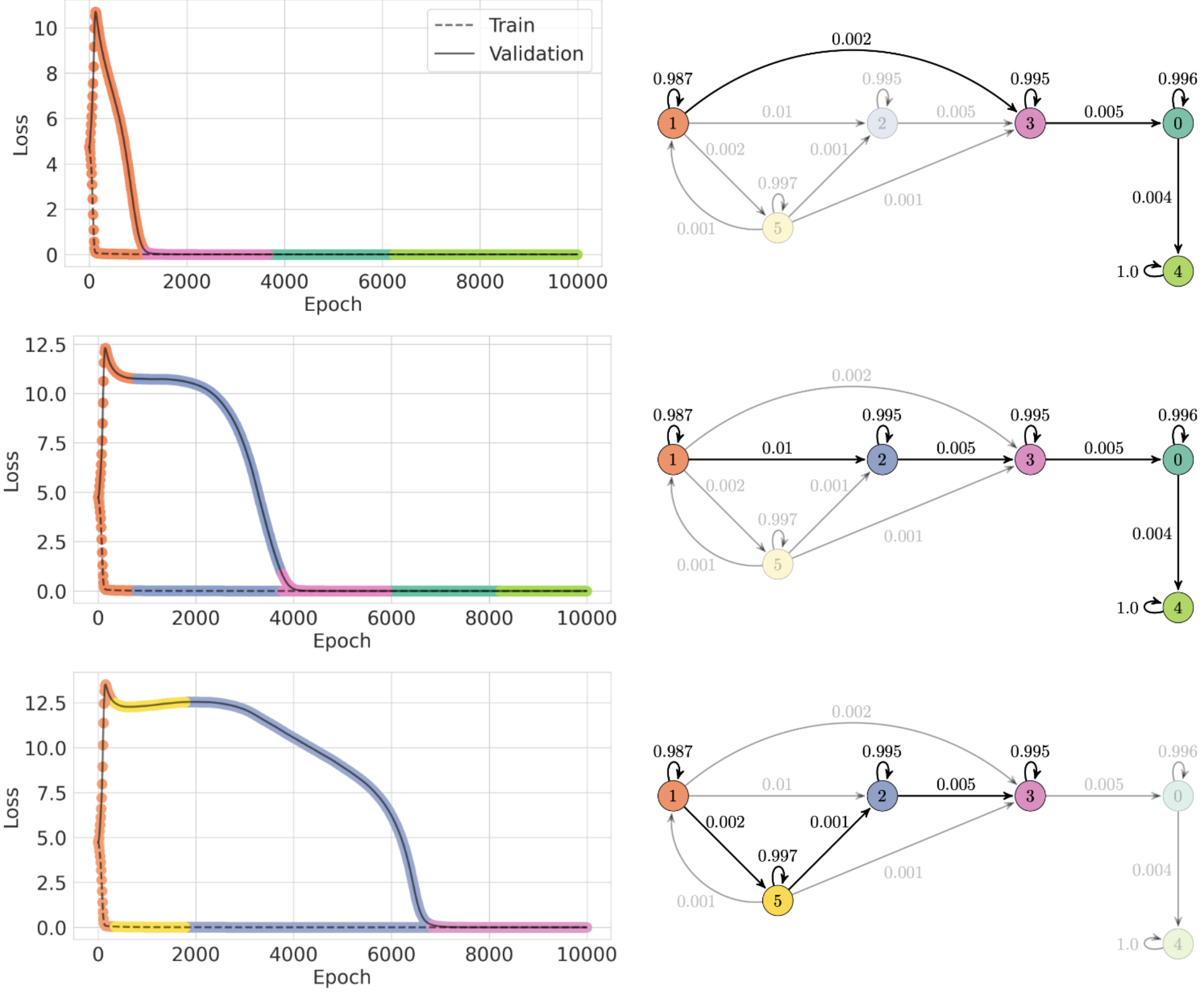

Edge	Top 3 important feature changes (z-score)	Transition frequency	Mean convergence epoch
$1 \rightarrow 3$	$L_2 \downarrow 1.68$, $\sigma(\mathbf{w}) \downarrow 1.99$, $L_1 \downarrow 1.83$	2 / 40	1810 ± 71.5
$1 \rightarrow 2$	$L_2 \downarrow 0.59$, $L_1 \downarrow 0.88$, $\frac{L_1}{L_2} \downarrow 1.05$	34 / 40	2950 ± 104
$1 \rightarrow 5$	$L_2 \downarrow 2.08$, $\sigma(\mathbf{w}) \downarrow 2.24$, $L_1 \downarrow 2.25$	4 / 40	5450 ± 313

Figure 2: One-layer transformer trained on modular addition. The first edge that a training run takes to exit the initialization state 1 significantly impacts the number of epochs the run takes to generalize. We sort features from most to least important by inverting the learned covariance matrices of each state, and we define edges by subtracting the learned means between states, as discussed in Section 2.2. See Appendix B for a glossary of metrics. The changes in the chart are the top three differences in learned means, sorted by importance–for example, state 2 has a learned L_2 norm that is 0.59 standard deviations lower than state 1, and the L_2 norm is the most important feature for state 2.

We examine several state transitions throughout training and find that the transitions are also characterized by similar changes between features.

3.3 Destabilizing Image Classification, Stabilizing Grokking

So far, we have observed that the training dynamics of neural networks learning algorithmic data (modular addition and sparse parities) are highly sensitive to random seed, while the dynamics of networks trained on

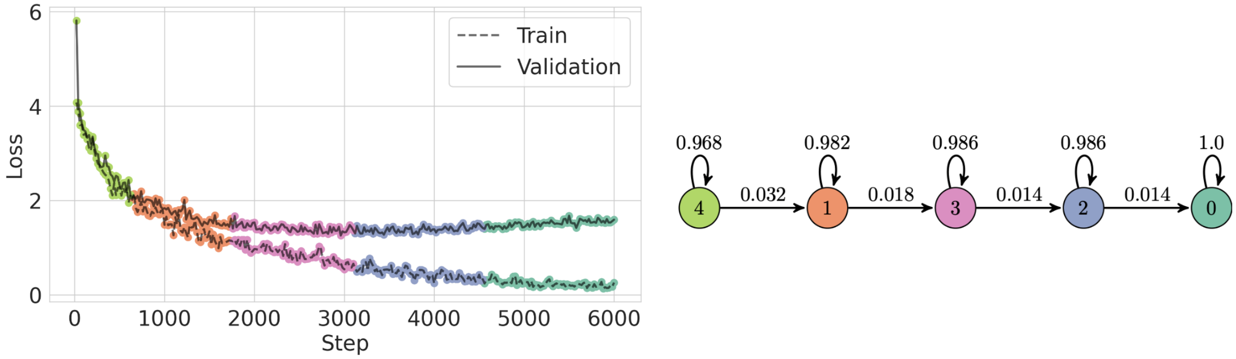

Edge	Top 3 important feature changes (z-score)
$4 \rightarrow 1$	$L_2 \uparrow 0.64$, $L_1 \uparrow 0.62$, $\mu(\lambda) \uparrow 0.56$
$1 \rightarrow 3$	$L_1 \uparrow 0.76$, $L_2 \uparrow 0.77$, $\mu(\lambda) \uparrow 0.75$
$3 \rightarrow 2$	$L_2 \uparrow 0.80$, $L_1 \uparrow 0.81$, $\mu(\lambda) \uparrow 0.83$
$2 \rightarrow 0$	$L_2 \uparrow 0.73$, $\mu(\lambda) \uparrow 0.75$, $L_1 \uparrow 0.73$

Figure 3: ResNet18 trained on CIFAR-100. All 40 training runs we collected from CIFAR-100 follow the same path, although individual runs can spend slightly different amounts of time in each state. As shown by the training map and accompanying annotations in the table, the training dynamics of CIFAR-100 are similar between states.

image classification are relatively unaffected by random seed. One possible explanation is that sensitivity to random seed is a property of the data, and grokking occurs because the data induces it. In this section, we will show that this explanation is incomplete. Rather, grokking is also affected by model architecture and optimization hyperparameters, and small changes to training can both close the gap between memorization and generalization in grokking and make training robust to changes in random seed.

First, we examine the training dynamics of ResNets without batch normalization (Ioffe & Szegedy, 2015) and residual connections. Residual connections help ResNets avoid vanishing gradients (He et al., 2016) and smooth the loss landscape (Li et al., 2018). Batch norm has similarly been shown to add smoothness to the loss landscape (Santurkar et al., 2018) and also contributes to automatic learning rate tuning (Arora et al., 2019). We remove batch norm and residual connections from ResNet18 and train the ablated networks from scratch on CIFAR-100 over 40 random seeds. All hyperparameters are in Appendix C.

Without batch norm and residual connections, ResNet18's training dynamics become significantly more sensitive to randomness. See Figure 4. Depending on the random seed, the model may stagnate for many updates before generalizing. This increase in random variation is visible in the learned training map, which now forks when exiting state 3, the initialization state. There now exists a slow-generalizing path ($3 \rightarrow 1$) and a fast-generalizing path ($3 \rightarrow 2$), characterized by feature movements in opposite directions. In the slow-generalizing path, norms and average singular value are increasing, while in the fast-generalizing path these features are slightly decreasing.

If removing batch normalization destabilizes ResNet training in CIFAR-100, then adding layer normalization (which was removed by Nanda et al. (2023)) should stabilize training in modular addition. Thus, we add layer normalization back in and train over 40 random seeds. We also decrease the batch size, which leads SGD to flatter minima (Keskar et al., 2017). These modifications to training help the transformer converge around 30 times faster on modular addition data. Furthermore, sensitivity to random seed disappears–the training map in Figure 5 becomes a linear graph.

From this section, we draw two conclusions. First, that grokking is caused by both the data and model training choices, and changes to model training can minimize the grokking effect. Second, that different hyperparameters or architectures can result in different training maps for the same task. In training setups

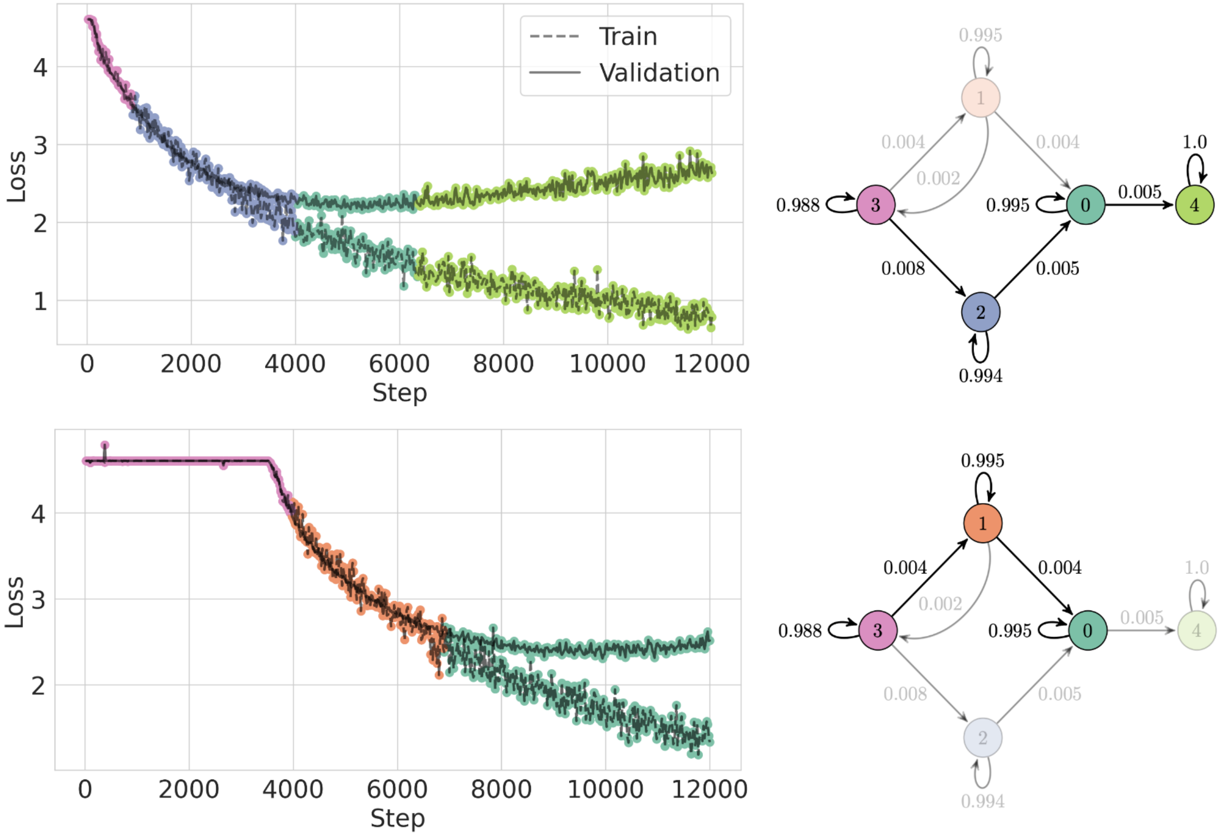

Edge	Top 3 important feature changes (z-score)	Transition frequency	Mean convergence step
$3 \to 2$	$L_2 \downarrow 0.10$, $\mu(\lambda) \downarrow 0.17$, $L_1 \downarrow 0.18$	29 / 40	3530 ± 460
$3 \to 1$	$\mu(\lambda) \uparrow 0.67$, $L_2 \uparrow 0.75$, $L_1 \uparrow 0.64$	12 / 40	7260 ± 3010

Figure 4: Without residual connections and batch normalization, ResNet training becomes unstable, causing convergence times to differ significantly. Slow-generalizing runs take the state transition ($3 \to 1$), while fast-generalizing runs take the state transition ($3 \to 2$). (Runs can take the path ($3 \to 1 \to 3 \to 2$), so transition frequencies do not sum to 40). The variability induced by removing residual connections and batch norm occurs at the beginning of training.

sensitive to random seed, the HMM associates differences in training dynamics with different latent states. We formalize the connection between latent states and metrics such as convergence time in the next section.

3.4 Predicting Convergence Time

We now use these state models as features in a linear regression to identify convergence time, as described in Section 2.3. We define convergence time as the iteration where validation accuracy is greater than some threshold, and we take this threshold to be 0.9 in modular addition and sparse parities, 0.6 for the stable version of CIFAR-100, 0.4 for destabilized CIFAR-100, and 0.97 for MNIST. We set these values to be slightly less than the maximum evaluation accuracy for each task, respectively. To visualize the variance in convergence times, see Appendix H.

In Table 1, we find that linear regression predicts convergence time from a given training run's distribution over latent states very accurately, as long as the training map contains forked paths. If the training map is instead linear, training follows similar paths through the HMM across different random seeds. We formalize this intuition of **trajectory dissimilarity** in terms of the expected Wasserstein distance $W(\cdot, \cdot)$

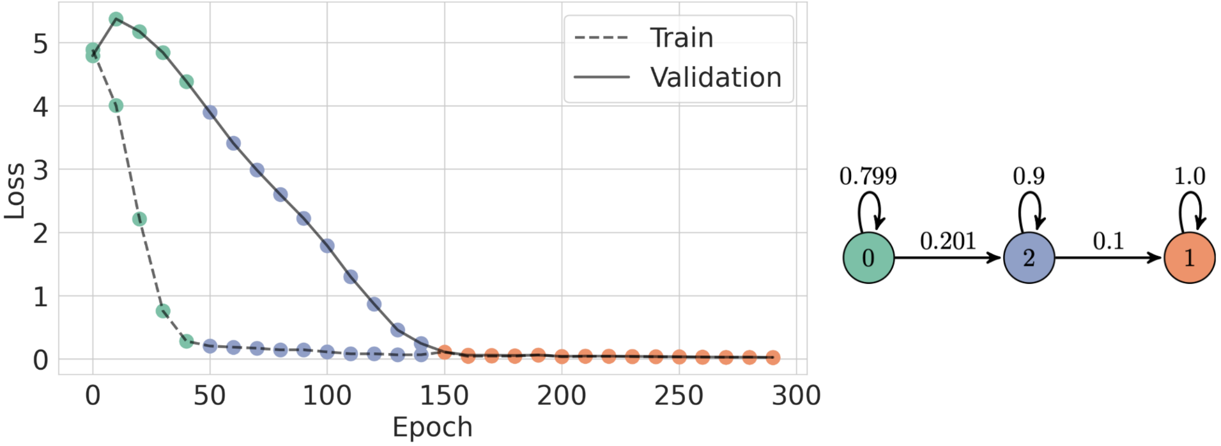

Edge	Top 3 important feature changes (z-score)
0 → 2	$L_2 \downarrow 0.52$, $L_1 \downarrow 0.93$, $\lambda_{max} \uparrow 0.92$
2 → 1	$L_2 \downarrow 2.08$, $\sigma(\mathbf{w}) \downarrow 2.24$, $L_1 \downarrow 2.25$

Figure 5: With layer normalization and a lower learning rate, the one-layer transformer quickly learns the modular arithmetic task, with a convergence time stable across random seed. This stability is captured by the linear training map. Critically, the map still reflects the grokking phase transitions: memorization, which occurs in state 0, and generalization, which occurs in state 2.

Dataset	R^2	p**-value**	**Dissimilarity**	**Forking**
Modular addition	0.977	<0.001	0.496	✓
Modular addition, stabilized	0.514	<0.001	0.038	
CIFAR-100	0.094	0.469	0.028	
CIFAR-100, destabilized	0.905	<0.001	0.806	✓
Sparse parities	0.961	<0.001	0.183	✓
MNIST	0.049	0.611	0.063	

Table 1: Predictability of convergence epoch using a unigram model of states. Dissimilarity is provided per Equation 3 and the training maps are marked as forking unless they are linear.

(Kantorovich, 1939; Vaserstein, 1969) between empirical distributions for any two random seeds p, q over latent states, sampled uniformly at random.

$$\text{Trajectory dissimilarity} := \mathbb{E}[W(p,q)] = \frac{2}{N(N-1)} \sum_{i=1}^{N} \sum_{j=1}^{i} W(p_i, q_j) \tag{3}$$

With statistically significant ($p < 0.001$) regression models for modular addition, sparse parities, and destabilized CIFAR-100, we can use the learned regression coefficients to find detour states. In Table 2, we highlight these detour states, defined as any state with a positive regression coefficient that is only visited by a strict subset of training trajectories. In our tasks with linear graphs, there are no detour states, because every training run visits every latent state. Our regression analysis largely confirms observations drawn from looking at the training maps and trajectories in sections prior: states 2 and 5 are detour states in modular addition, state 0 is a detour state in sparse parities, and state 1 is a detour state in destabilized CIFAR-100.

Detour states signal that the outcome of training is unstable: they appear in training setups that are sensitive to randomness, and they disappear in setups that are robust to randomness. By adding layer norm and decreasing batch size, we decreased both the mean and variance of convergence time in modular addition

State	Coefficient
0	-0.15
1	0.98
2	**1.19**
3	-0.20
4	0.18
5	**0.95**

(a) Modular addition

State	Coefficient
0	**0.77**
1	0.41
2	0.98
3	-0.23
4	0.58
5	1.13

(b) Sparse parities

State	Coefficient
0	0.66
1	**1.20**
2	0.28
3	1.91
4	1.12

(c) CIFAR-100, destabilized

Table 2: Learned linear regression coefficients. If the value is positive, then the time spent in the state is correlated with increased convergence time, and vice versa. Detour states are bolded.

(see Table 1). Under these stabilized regimes, detour states disappear, as the training map becomes a linear graph. Conversely, removing batch norm and residual connections destabilizes the training of ResNets, thereby inducing forks in the training map that lead to detour states.

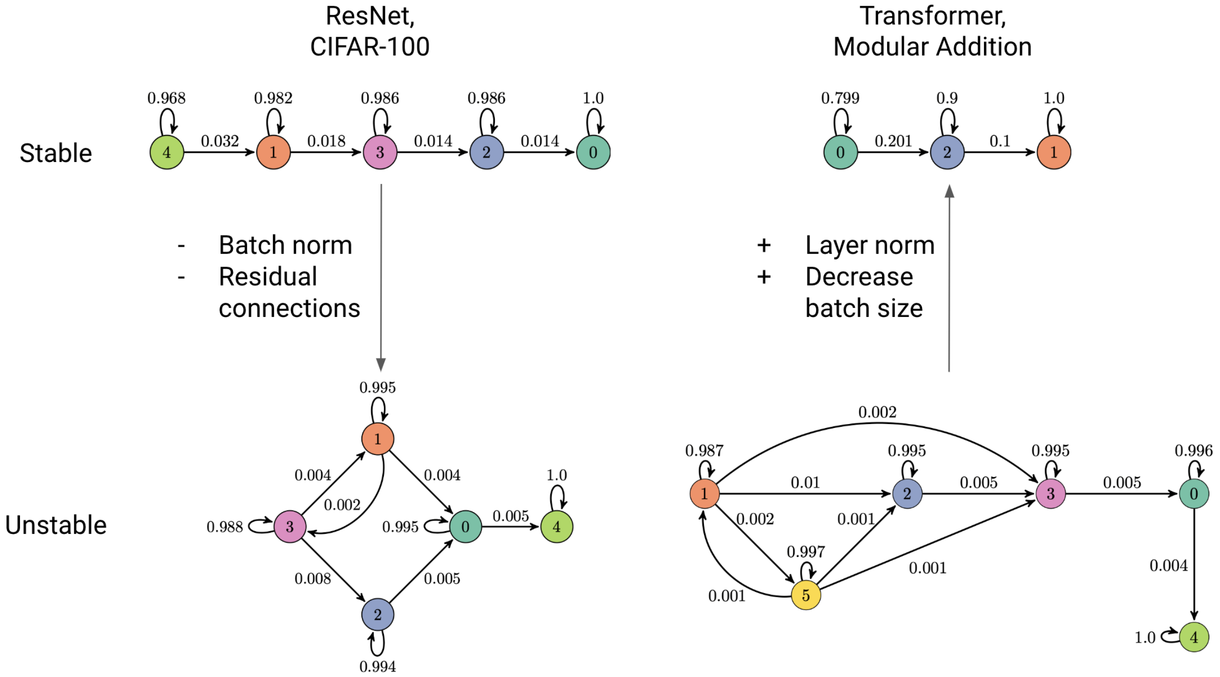

Figure 6: Training maps express variability in training dynamics as a more densely connected graph. For stable training setups, the HMM learns a linear graph as the training map. Training dynamics can be stabilized or destabilized by changing hyperparameters (batch size) or architecture (normalization layers, residual connections).

4 Related Work

Our work is not the first to relate state machines to the internals of a neural network. Weiss et al. (2018; 2019) extract deterministic finite automata (DFA) from neural networks, which bears some similarity to the annotated Markov chain we extract from training runs. Williams (1992) use an extended Kalman filter (EKF) to train a recurrent neural network and note the similarity between EKF and the real-time recurrent learning algorithm (Marschall et al., 2020). In contrast to the existing literature, we use state machines to understand the training process rather than the inference process. Measuring the state of a neural network using various metrics was also done in Frankle et al. (2020).

Analyzing time series data using a probabilistic framework has been successfully applied to many other tasks in machine learning (Kim et al., 2017; Hughey & Krogh, 1996; Bartolucci et al., 2014). In a similar spirit to our work, Batty et al. (2019) use an autoregressive HMM (ARHMM) to segment behavioral videos into semantically similar chunks. The ARHMM can capture both discrete and continuous latent dynamics, making it an interesting model to try for future work. These modeling decisions (discrete vs. continuous latent space, dimensionality reduction) all impact the interpretation of the trained model, so we invite readers to consider them carefully.

Our work is substantively inspired by the progress measures literature, which aims to find metrics that can predict discontinuous improvement or convergence in neural networks. Barak et al. (2022) first hypothesized the existence of hidden progress measures. Olsson et al. (2022) found a progress measure for induction heads in Transformer-based language models, and Nanda et al. (2023) found a progress measure for grokking in the modular arithmetic task. The L_2 norm is also known to be both important to and predictive of grokking, thereby motivating the use of weight decay to accelerate convergence in grokking settings (Nanda et al., 2023; Power et al., 2022; Thilak et al., 2022). Liu et al. (2023) highlight the importance of the L_2 norm by correcting for grokking via projected gradient descent within a fixed-size L_2 ball; conversely, they also induce grokking on new datasets by choosing a disadvantageous L_2 norm. Our results mirror their work while showing that grokking has other available remedies, beyond ones that directly manipulate the L_2 norm.

Finally, this work relates broadly to the empirical study of training dynamics. Much of the literature treats learning as a process where increases in training data lead to predictable increases in test performance (Kaplan et al., 2020; Razeghi et al., 2022) and in model complexity (Choshen et al., 2022; Mangalam & Prabhu, 2019; Nakkiran et al., 2019). However, this treatment of training ignores how heterogeneous the factors of training can be. Different capabilities are learned at different rates (Srivastava et al., 2022), different layers converge at different rates (Raghu et al., 2017), and different latent dimensions emerge at different rates (Jarvis et al., 2023; Saxe et al., 2019). While early stages in training can be modeled nearly exactly through simple methods (Hu et al., 2020; Jacot et al., 2018), these early stages are notably distinct from later stages. Early stages exhibit unique phenomena such as critical learning periods (Achille et al., 2019) and break-even points (Jastrzebski et al., 2020). Consequently, methods like ours which treat training as a heterogeneous process are crucial in understanding realistic training trajectories.

5 Discussion

The training maps derived from HMMs are interpretable descriptions of training dynamics that summarize similarities and differences between training runs. Our results show that there exists a low-dimensional, *discrete* representation of training dynamics. Via the HMM, this representation is generally predictive of the next set of metrics in the training trajectory, given the previous metrics. Furthermore, in some cases this low-dimensional, discrete representation can even be used to predict the iteration in which models converge.

5.1 Grokking and the Optimization Landscape

We conjecture that grokking is the consequence of a sharp optimization landscape. Consider the edits we performed to significantly decrease the grokking effect: adding layer normalization and decreasing batch size. Normalization layers and decreasing batch size have been documented in the literature as increasing smoothness in the loss landscape (Santurkar et al., 2018; Arora et al., 2019; Keskar et al., 2017). Image classification is a well-studied task with many tricks for improving the efficiency of training; perhaps learning algorithmic data will become just as efficient in the future, such that grokking is no longer a concern.

5.2 Progress Measures and Phase Transitions

By modeling convergence time in grokking settings, we analyze phase transitions. We find that the generalization phase transition can be sped up by avoiding detour states. These detour states are generally characterized by specific requirements in metrics such as the L_2 norm. For example, in the modular arithmetic setting, avoiding detour states requires a “just-right” decrease in the L_2 norm–not too little, and not too much. Liu et al. (2023) posited that grokking occurs because the weight norm is slow to reach a shell of particular L_2 norm in weight space, previously called the “Goldilocks zone” (Fort & Scherlis, 2018); our results suggest that the rate of change is also crucial, and not only the momentary value of the norm.

5.3 The Impact of Random Seed

We recommend that researchers studying training dynamics experiment with a large number of training seeds. When claims are based on a small number of runs, anomalous training phenomena might be missed, simply due to sampling. These anomalous phenomena can be the most elucidating, as in grokking experiments, where a small number of runs converge faster than the rest. The role of random variation has been highlighted for the performance and generalization of trained models (McCoy et al., 2020; Sellam et al., 2022; Juneja et al., 2023), but there are fewer studies on variation in training dynamics. We recommend studying training across many runs, and possibly relying on state diagrams like ours to distinguish typical and anomalous training phenomena.

5.4 Limitations and Future Work

Our work assumes that training dynamics can be represented by a linear, discrete, and Markovian model. Despite the successes of our approach, a higher-powered model might capture even more information about training dynamics. Relaxing the assumptions of the HMM is likely a fruitful area for future work. Additionally, in this work we perform dimensionality reduction via hand-picked statistics. We use these statistics as interpretable features for our training maps, but a fully unsupervised approach also deserves exploration. Finally, our findings are suggestive for future work on hyperparameter search. We demonstrate that 1) training instability to random seed is highly dependent on hyperparameters, and 2) instability manifests early in training. Thus, it may be more efficient to measure early variation across a few seeds to quickly evaluate a hyperparameter setting, rather than waiting to measure accuracy on the trained model.

6 Conclusion

We make several main contributions. First, we propose directly modeling training dynamics as a new avenue for interpretability and training dynamics research. We show that even with a simple model like the HMM, we can learn representations of training dynamics that are predictive of key metrics like convergence time. Second, we discover detour states of learning, and show that detour states are related to both how quickly models converge and how sensitive the overall training process is to random seed. Finally, we show that stability across random seeds is empirically linked to generalization, providing a possible criterion for model tuning and selection.

References

Alessandro Achille, Matteo Rovere, and Stefano Soatto. Critical Learning Periods in Deep Neural Networks. *arXiv:1711.08856 [cs, q-bio, stat]*, February 2019. URL `http://arxiv.org/abs/1711.08856`. arXiv: 1711.08856.

Hirotogu Akaike. *Information Theory and an Extension of the Maximum Likelihood Principle*, pp. 199–213. Springer New York, New York, NY, 1998. ISBN 978-1-4612-1694-0. doi: 10.1007/978-1-4612-1694-0_15. URL `https://doi.org/10.1007/978-1-4612-1694-0_15`.

Sanjeev Arora, Zhiyuan Li, and Kaifeng Lyu. Theoretical analysis of auto rate-tuning by batch normalization. In *International Conference on Learning Representations*, 2019. URL `https://openreview.net/forum?id=rkxQ-nA9FX`.

Boaz Barak, Benjamin L. Edelman, Surbhi Goel, Sham M. Kakade, eran malach, and Cyril Zhang. Hidden progress in deep learning: SGD learns parities near the computational limit. In Alice H. Oh, Alekh Agarwal, Danielle Belgrave, and Kyunghyun Cho (eds.), *Advances in Neural Information Processing Systems*, 2022. URL `https://openreview.net/forum?id=8XWP2ewX-im`.

Francesco Bartolucci, Alessio Farcomeni, and Fulvia Pennoni. Latent markov models: a review of a general framework for the analysis of longitudinal data with covariates. *TEST*, 23:433–465, 2014.

Eleanor Batty, Matthew R Whiteway, Shreya Saxena, Dan Biderman, Taiga Abe, Simon Musall, Winthrop F. Gillis, Jeffrey E. Markowitz, Anne K. Churchland, John P. Cunningham, Sandeep Robert Datta, Scott W. Linderman, and Liam Paninski. Behavenet: nonlinear embedding and bayesian neural decoding of behavioral videos. In *Neural Information Processing Systems*, 2019.

Leonard E. Baum and Ted Petrie. Statistical Inference for Probabilistic Functions of Finite State Markov Chains. *The Annals of Mathematical Statistics*, 37(6):1554 – 1563, 1966. doi: 10.1214/aoms/1177699147. URL `https://doi.org/10.1214/aoms/1177699147`.

Leonard E. Baum, Ted Petrie, George W. Soules, and Norman Weiss. A maximization technique occurring in the statistical analysis of probabilistic functions of markov chains. *Annals of Mathematical Statistics*, 41:164–171, 1970.

Leshem Choshen, Guy Hacohen, Daphna Weinshall, and Omri Abend. The Grammar-Learning Trajectories of Neural Language Models. *arXiv:2109.06096 [cs]*, March 2022. URL `http://arxiv.org/abs/2109.06096`. arXiv: 2109.06096.

Jacob Devlin, Ming-Wei Chang, Kenton Lee, and Kristina Toutanova. BERT: Pre-training of deep bidirectional transformers for language understanding. In *Proceedings of the 2019 Conference of the North American Chapter of the Association for Computational Linguistics: Human Language Technologies, Volume 1 (Long and Short Papers)*, pp. 4171–4186, Minneapolis, Minnesota, June 2019. Association for Computational Linguistics. doi: 10.18653/v1/N19-1423. URL `https://aclanthology.org/N19-1423`.

Stanislav Fort and Adam Scherlis. The goldilocks zone: Towards better understanding of neural network loss landscapes. *CoRR*, abs/1807.02581, 2018. URL `http://arxiv.org/abs/1807.02581`.

Jonathan Frankle, David J. Schwab, and Ari S. Morcos. The early phase of neural network training. In *International Conference on Learning Representations*, 2020. URL `https://openreview.net/forum?id=Hkl1iRNFwS`.

Tomer Galanti, Zachary S. Siegel, Aparna Gupte, and Tomaso Poggio. Sgd and weight decay provably induce a low-rank bias in neural networks, 2023.

Elad Hazan. Introduction to online convex optimization. *CoRR*, abs/1909.05207, 2019. URL `http://arxiv.org/abs/1909.05207`.

Kaiming He, Xiangyu Zhang, Shaoqing Ren, and Jian Sun. Deep residual learning for image recognition. In *2016 IEEE Conference on Computer Vision and Pattern Recognition (CVPR)*, pp. 770–778, 2016. doi: 10.1109/CVPR.2016.90.

Wei Hu, L. Xiao, Ben Adlam, and Jeffrey Pennington. The Surprising Simplicity of the Early-Time Learning Dynamics of Neural Networks. *ArXiv*, 2020.

Richard Hughey and Anders Krogh. Hidden markov models for sequence analysis: extension and analysis of the basic method. *Computer applications in the biosciences : CABIOS*, 12 2:95–107, 1996.

Niall P. Hurley and Scott T. Rickard. Comparing measures of sparsity. *IEEE Transactions on Information Theory*, 55:4723–4741, 2008.

Sergey Ioffe and Christian Szegedy. Batch normalization: Accelerating deep network training by reducing internal covariate shift. In Francis Bach and David Blei (eds.), *Proceedings of the 32nd International Conference on Machine Learning*, volume 37 of *Proceedings of Machine Learning Research*, pp. 448–456, Lille, France, 07–09 Jul 2015. PMLR. URL `https://proceedings.mlr.press/v37/ioffe15.html`.

Arthur Jacot, Franck Gabriel, and Clément Hongler. Neural Tangent Kernel: Convergence and Generalization in Neural Networks. *arXiv:1806.07572 [cs, math, stat]*, June 2018. URL `http://arxiv.org/abs/1806.07572`. arXiv: 1806.07572.

Devon Jarvis, Richard Klein, Benjamin Rosman, and Andrew M Saxe. On the specialization of neural modules. In *The Eleventh International Conference on Learning Representations*, 2023. URL `https://openreview.net/forum?id=Fh97BDaR6I`.

Stanislaw Jastrzebski, Maciej Szymczak, Stanislav Fort, Devansh Arpit, Jacek Tabor, Kyunghyun Cho, and Krzysztof Geras. The Break-Even Point on Optimization Trajectories of Deep Neural Networks. *arXiv:2002.09572 [cs, stat]*, February 2020. URL `http://arxiv.org/abs/2002.09572`. arXiv: 2002.09572.

Jeevesh Juneja, Rachit Bansal, Kyunghyun Cho, João Sedoc, and Naomi Saphra. Linear connectivity reveals generalization strategies. In *The Eleventh International Conference on Learning Representations*, 2023. URL `https://openreview.net/forum?id=hY6M0JHl3uL`.

Leonid V Kantorovich. Mathematical methods of organizing and planning production. *Management science*, 6(4), 1939.

Jared Kaplan, Sam McCandlish, Tom Henighan, Tom B. Brown, Benjamin Chess, Rewon Child, Scott Gray, Alec Radford, Jeffrey Wu, and Dario Amodei. Scaling Laws for Neural Language Models. *arXiv:2001.08361 [cs, stat]*, January 2020. URL `http://arxiv.org/abs/2001.08361`. arXiv: 2001.08361.

Nitish Shirish Keskar, Dheevatsa Mudigere, Jorge Nocedal, Mikhail Smelyanskiy, and Ping Tak Peter Tang. On large-batch training for deep learning: Generalization gap and sharp minima. In *International Conference on Learning Representations*, 2017. URL `https://openreview.net/forum?id=H1oyRlYgg`.

Bomin Kim, Kevin H. Lee, Lingzhou Xue, and Xiaoyue Niu. A review of dynamic network models with latent variables. *Statistics surveys*, 12:105–135, 2017.

Alex Krizhevsky. Learning multiple layers of features from tiny images. Master's thesis, University of Toronto, 2009. URL `https://api.semanticscholar.org/CorpusID:18268744`.

Hao Li, Zheng Xu, Gavin Taylor, and Tom Goldstein. Visualizing the loss landscape of neural nets, 2018. URL `https://openreview.net/forum?id=HkmaTz-0W`.

Ziming Liu, Eric J Michaud, and Max Tegmark. Omnigrok: Grokking beyond algorithmic data. In *The Eleventh International Conference on Learning Representations*, 2023. URL `https://openreview.net/forum?id=zDiHoIWa0q1`.

Kaifeng Lyu, Zhiyuan Li, and Sanjeev Arora. Understanding the generalization benefit of normalization layers: Sharpness reduction. In Alice H. Oh, Alekh Agarwal, Danielle Belgrave, and Kyunghyun Cho (eds.), *Advances in Neural Information Processing Systems*, 2022. URL `https://openreview.net/forum?id=xp5VOBxTxZ`.

Pranava Madhyastha and Rishabh Jain. On model stability as a function of random seed. In *Proceedings of the 23rd Conference on Computational Natural Language Learning (CoNLL)*, pp. 929–939, Hong Kong, China, November 2019. Association for Computational Linguistics. doi: 10.18653/v1/K19-1087. URL `https://aclanthology.org/K19-1087`.

Karttikeya Mangalam and Vinay Uday Prabhu. Do deep neural networks learn shallow learnable examples first? *ICML 2019 Workshop on Identifying and Understanding Deep Learning Phenomena*, 2019. URL `https://openreview.net/forum?id=HkxHv4rn24`.

Owen Marschall, Kyunghyun Cho, and Cristina Savin. A unified framework of online learning algorithms for training recurrent neural networks. *J. Mach. Learn. Res.*, 21(1), jan 2020. ISSN 1532-4435.

R. Thomas McCoy, Junghyun Min, and Tal Linzen. BERTs of a feather do not generalize together: Large variability in generalization across models with similar test set performance. In *Proceedings of the Third BlackboxNLP Workshop on Analyzing and Interpreting Neural Networks for NLP*, pp. 217–227, Online, November 2020. Association for Computational Linguistics. doi: 10.18653/v1/2020.blackboxnlp-1.21. URL `https://aclanthology.org/2020.blackboxnlp-1.21`.

Preetum Nakkiran, Gal Kaplun, Dimitris Kalimeris, Tristan Yang, Benjamin L. Edelman, Fred Zhang, and Boaz Barak. SGD on Neural Networks Learns Functions of Increasing Complexity. *arXiv:1905.11604 [cs, stat]*, May 2019. URL `http://arxiv.org/abs/1905.11604`. arXiv: 1905.11604.

Neel Nanda, Lawrence Chan, Tom Lieberum, Jess Smith, and Jacob Steinhardt. Progress measures for grokking via mechanistic interpretability. In *The Eleventh International Conference on Learning Representations*, 2023. URL `https://openreview.net/forum?id=9XFSbDPmdW`.

Catherine Olsson, Nelson Elhage, Neel Nanda, Nicholas Joseph, Nova DasSarma, Tom Henighan, Ben Mann, Amanda Askell, Yuntao Bai, Anna Chen, Tom Conerly, Dawn Drain, Deep Ganguli, Zac Hatfield-Dodds, Danny Hernandez, Scott Johnston, Andy Jones, Jackson Kernion, Liane Lovitt, Kamal Ndousse, Dario Amodei, Tom Brown, Jack Clark, Jared Kaplan, Sam McCandlish, and Chris Olah. In-context learning and induction heads, 2022.

Alethea Power, Yuri Burda, Harrison Edwards, Igor Babuschkin, and Vedant Misra. Grokking: Generalization beyond overfitting on small algorithmic datasets. *CoRR*, abs/2201.02177, 2022. URL `https://arxiv.org/abs/2201.02177`.

Maithra Raghu, Justin Gilmer, Jason Yosinski, and Jascha Sohl-Dickstein. SVCCA: Singular Vector Canonical Correlation Analysis for Deep Learning Dynamics and Interpretability. *arXiv:1706.05806 [cs, stat]*, June 2017. URL `http://arxiv.org/abs/1706.05806`. arXiv: 1706.05806.

Yasaman Razeghi, Robert L Logan IV, Matt Gardner, and Sameer Singh. Impact of Pretraining Term Frequencies on Few-Shot Numerical Reasoning. In *Findings of the Association for Computational Linguistics: EMNLP 2022*, pp. 840–854, Abu Dhabi, United Arab Emirates, December 2022. Association for Computational Linguistics. URL `https://aclanthology.org/2022.findings-emnlp.59`.

Shibani Santurkar, Dimitris Tsipras, Andrew Ilyas, and Aleksander Mądry. How does batch normalization help optimization? In *Proceedings of the 32nd International Conference on Neural Information Processing Systems*, NIPS'18, pp. 2488–2498, Red Hook, NY, USA, 2018. Curran Associates Inc.

Andrew M. Saxe, James L. McClelland, and Surya Ganguli. A mathematical theory of semantic development in deep neural networks. *Proceedings of the National Academy of Sciences*, 116(23):11537–11546, June 2019. ISSN 0027-8424, 1091-6490. doi: 10.1073/pnas.1820226116. URL `https://www.pnas.org/content/116/23/11537`. Publisher: National Academy of Sciences Section: PNAS Plus.

Gideon Schwarz. Estimating the dimension of a model. *Annals of Statistics*, 6:461–464, 1978.

Thibault Sellam, Steve Yadlowsky, Ian Tenney, Jason Wei, Naomi Saphra, Alexander D'Amour, Tal Linzen, Jasmijn Bastings, Iulia Raluca Turc, Jacob Eisenstein, Dipanjan Das, and Ellie Pavlick. The multiBERTs: BERT reproductions for robustness analysis. In *International Conference on Learning Representations*, 2022. URL `https://openreview.net/forum?id=K0E_F0gFDgA`.

Patrice Y. Simard, Dave Steinkraus, and John Platt. Best practices for convolutional neural networks applied to visual document analysis. In *Seventh International Conference on Document Analysis and Recognition, 2003. Proceedings.*, pp. 958–963, 2003. doi: 10.1109/ICDAR.2003.1227801.

Samuel L Smith, Benoit Dherin, David Barrett, and Soham De. On the origin of implicit regularization in stochastic gradient descent. In *International Conference on Learning Representations*, 2021. URL `https://openreview.net/forum?id=rq_Qr0c1Hyo`.

Aarohi Srivastava, Abhinav Rastogi, Abhishek Rao, Abu Awal Md Shoeb, Abubakar Abid, Adam Fisch, Adam R. Brown, Adam Santoro, Aditya Gupta, Adrià Garriga-Alonso, Agnieszka Kluska, Aitor Lewkowycz, Akshat Agarwal, Alethea Power, Alex Ray, Alex Warstadt, Alexander W. Kocurek, Ali Safaya, Ali Tazarv, Alice Xiang, Alicia Parrish, Allen Nie, Aman Hussain, Amanda Askell, Amanda Dsouza, Ambrose Slone, Ameet Rahane, Anantharaman S. Iyer, Anders Andreassen, Andrea Madotto, Andrea Santilli, Andreas Stuhlmüller, Andrew Dai, Andrew La, Andrew Lampinen, Andy Zou, Angela Jiang, Angelica Chen, Anh Vuong, Animesh Gupta, Anna Gottardi, Antonio Norelli, Anu Venkatesh, Arash Gholamidavoodi, Arfa Tabassum, Arul Menezes, Arun Kirubarajan, Asher Mullokandov, Ashish Sabharwal, Austin Herrick, Avia Efrat, Aykut Erdem, Ayla Karakaş, B. Ryan Roberts, Bao Sheng Loe, Barret Zoph, Bartłomiej Bojanowski, Batuhan Özyurt, Behnam Hedayatnia, Behnam Neyshabur, Benjamin Inden, Benno Stein, Berk Ekmekci, Bill Yuchen Lin, Blake Howald, Cameron Diao, Cameron Dour, Catherine Stinson, Cedrick Argueta, César Ferri Ramírez, Chandan Singh, Charles Rathkopf, Chenlin Meng, Chitta Baral, Chiyu Wu, Chris Callison-Burch, Chris Waites, Christian Voigt, Christopher D. Manning, Christopher Potts, Cindy Ramirez, Clara E. Rivera, Clemencia Siro, Colin Raffel, Courtney Ashcraft, Cristina Garbacea, Damien Sileo, Dan Garrette, Dan Hendrycks, Dan Kilman, Dan Roth, Daniel Freeman, Daniel Khashabi, Daniel Levy, Daniel Moseguí González, Danielle Perszyk, Danny Hernandez, Danqi Chen, Daphne Ippolito, Dar Gilboa, David Dohan, David Drakard, David Jurgens, Debajyoti Datta, Deep Ganguli, Denis Emelin, Denis Kleyko, Deniz Yuret, Derek Chen, Derek Tam, Dieuwke Hupkes, Diganta Misra, Dilyar Buzan, Dimitri Coelho Mollo, Diyi Yang, Dong-Ho Lee, Ekaterina Shutova, Ekin Dogus Cubuk, Elad Segal, Eleanor Hagerman, Elizabeth Barnes, Elizabeth Donoway, Ellie Pavlick, Emanuele Rodola, Emma Lam, Eric Chu, Eric Tang, Erkut Erdem, Ernie Chang, Ethan A. Chi, Ethan Dyer, Ethan Jerzak, Ethan Kim, Eunice Engefu Manyasi, Evgenii Zheltonozhskii, Fanyue Xia, Fatemeh Siar, Fernando Martínez-Plumed, Francesca Happé, Francois Chollet, Frieda Rong, Gaurav Mishra, Genta Indra Winata, Gerard de Melo, Germán Kruszewski, Giambattista Parascandolo, Giorgio Mariani, Gloria Wang, Gonzalo Jaimovitch-López, Gregor Betz, Guy Gur-Ari, Hana Galijasevic, Hannah Kim, Hannah Rashkin, Hannaneh Hajishirzi, Harsh Mehta, Hayden Bogar, Henry Shevlin, Hinrich Schütze, Hiromu Yakura, Hongming Zhang, Hugh Mee Wong, Ian Ng, Isaac Noble, Jaap Jumelet, Jack Geissinger, Jackson Kernion, Jacob Hilton, Jaehoon Lee, Jaime Fernández Fisac, James B. Simon, James Koppel, James Zheng, James Zou, Jan Kocoń, Jana Thompson, Jared Kaplan, Jarema Radom, Jascha Sohl-Dickstein, Jason Phang, Jason Wei, Jason Yosinski, Jekaterina Novikova, Jelle Bosscher, Jennifer Marsh, Jeremy Kim, Jeroen Taal, Jesse Engel, Jesujoba Alabi, Jiacheng Xu, Jiaming Song, Jillian Tang, Joan Waweru, John Burden, John Miller, John U. Balis, Jonathan Berant, Jörg Frohberg, Jos Rozen, Jose Hernandez-Orallo, Joseph Boudeman, Joseph Jones, Joshua B. Tenenbaum, Joshua S. Rule, Joyce Chua, Kamil Kanclerz, Karen Livescu, Karl Krauth, Karthik Gopalakrishnan, Katerina Ignatyeva, Katja Markert, Kaustubh D. Dhole, Kevin Gimpel, Kevin Omondi, Kory Mathewson, Kristen Chiafullo, Ksenia Shkaruta, Kumar Shridhar, Kyle McDonell, Kyle Richardson, Laria Reynolds, Leo Gao, Li Zhang, Liam Dugan, Lianhui Qin, Lidia Contreras-Ochando, Louis-Philippe Morency, Luca Moschella, Lucas Lam, Lucy Noble, Ludwig Schmidt, Luheng He, Luis Oliveros Colón, Luke Metz, Lütfi Kerem Şenel, Maarten Bosma, Maarten Sap, Maartje ter Hoeve, Maheen Farooqi, Manaal Faruqui, Mantas Mazeika, Marco Baturan, Marco Marelli, Marco Maru, Maria Jose Ramírez Quintana, Marie Tolkiehn, Mario Giulianelli, Martha Lewis, Martin Potthast, Matthew L. Leavitt, Matthias Hagen, Mátyás Schubert, Medina Orduna Baitemirova, Melody Arnaud, Melvin McElrath, Michael A. Yee, Michael Cohen, Michael Gu, Michael Ivanitskiy, Michael Starritt, Michael Strube, Michał Swędrowski, Michele Bevilacqua, Michihiro Yasunaga, Mihir Kale, Mike Cain, Mimee Xu, Mirac Suzgun, Mo Tiwari, Mohit Bansal, Moin Aminnaseri, Mor Geva, Mozhdeh Gheini, Mukund Varma T, Nanyun Peng, Nathan Chi, Nayeon Lee, Neta Gur-Ari Krakover, Nicholas Cameron, Nicholas Roberts, Nick Doiron, Nikita Nangia, Niklas Deckers, Niklas Muennighoff, Nitish Shirish Keskar, Niveditha S. Iyer, Noah Constant, Noah Fiedel, Nuan Wen, Oliver Zhang, Omar Agha, Omar Elbaghdadi, Omer Levy, Owain Evans, Pablo Antonio Moreno Casares, Parth Doshi, Pascale Fung, Paul Pu Liang, Paul Vicol, Pegah Alipoormolabashi, Peiyuan Liao, Percy Liang, Peter Chang, Peter Eckersley, Phu Mon Htut, Pinyu Hwang, Piotr Miłkowski, Piyush Patil, Pouya Pezeshkpour, Priti Oli, Qiaozhu Mei, Qing Lyu, Qinlang Chen, Rabin Banjade, Rachel Etta Rudolph, Raefer Gabriel, Rahel Habacker, Ramón Risco Delgado, Raphaël Millière, Rhythm Garg, Richard Barnes, Rif A. Saurous, Riku Arakawa, Robbe Raymaekers, Robert Frank, Rohan Sikand, Roman Novak, Roman Sitelew, Ronan LeBras, Rosanne Liu, Rowan Jacobs, Rui Zhang, Ruslan Salakhutdinov, Ryan Chi, Ryan Lee, Ryan Stovall, Ryan Teehan, Rylan Yang, Sahib Singh, Saif M. Mohammad, Sajant Anand, Sam Dillavou, Sam Shleifer, Sam Wiseman, Samuel Gruetter, Samuel R. Bowman, Samuel S. Schoenholz, Sanghyun Han, Sanjeev Kwatra, Sarah A. Rous, Sarik Ghazarian, Sayan Ghosh, Sean Casey, Sebastian Bischoff, Sebastian Gehrmann, Sebastian Schuster, Sepideh Sadeghi, Shadi Hamdan, Sharon Zhou, Shashank Srivastava, Sherry Shi, Shikhar Singh, Shima Asaadi, Shixiang Shane Gu, Shubh Pachchigar, Shubham Toshniwal, Shyam Upadhyay, Shyamolima, Debnath, Siamak Shakeri, Simon Thormeyer, Simone Melzi, Siva Reddy, Sneha Priscilla Makini, Soo-Hwan Lee, Spencer Torene, Sriharsha Hatwar, Stanislas Dehaene, Stefan Divic, Stefano Ermon, Stella Biderman, Stephanie Lin, Stephen Prasad, Steven T. Piantadosi, Stuart M. Shieber, Summer Misherghi, Svetlana Kiritchenko, Swaroop Mishra, Tal Linzen, Tal Schuster, Tao Li, Tao Yu, Tariq Ali, Tatsu Hashimoto, Te-Lin Wu, Théo Desbordes, Theodore Rothschild, Thomas Phan, Tianle Wang, Tiberius Nkinyili, Timo Schick, Timofei Kornev, Timothy Telleen-Lawton, Titus Tunduny, Tobias Gerstenberg, Trenton Chang, Trishala Neeraj, Tushar Khot, Tyler Shultz, Uri Shaham, Vedant Misra, Vera Demberg, Victoria Nyamai, Vikas Raunak, Vinay Ramasesh, Vinay Uday Prabhu, Vishakh Padmakumar, Vivek Srikumar, William Fedus, William Saunders, William Zhang, Wout Vossen, Xiang Ren, Xiaoyu Tong, Xinran Zhao, Xinyi Wu, Xudong Shen, Yadollah Yaghoobzadeh, Yair Lakretz, Yangqiu Song, Yasaman Bahri, Yejin Choi, Yichi Yang, Yiding Hao, Yifu Chen, Yonatan Belinkov, Yu Hou, Yufang Hou, Yuntao Bai, Zachary Seid, Zhuoye Zhao, Zijian Wang, Zijie J. Wang, Zirui Wang, and Ziyi Wu. Beyond the Imitation Game: Quantifying and extrapolating the capabilities of language models, June 2022. URL `http://arxiv.org/abs/2206.04615`. Number: arXiv:2206.04615 arXiv:2206.04615 [cs, stat].

Vimal Thilak, Etai Littwin, Shuangfei Zhai, Omid Saremi, Roni Paiss, and Joshua Susskind. The slingshot mechanism: An empirical study of adaptive optimizers and the grokking phenomenon, 2022.

Leonid Nisonovich Vaserstein. Markov processes over denumerable products of spaces, describing large systems of automata. *Problemy Peredachi Informatsii*, 5(3):64–72, 1969.

Gail Weiss, Yoav Goldberg, and Eran Yahav. Extracting automata from recurrent neural networks using queries and counterexamples. In Jennifer Dy and Andreas Krause (eds.), *Proceedings of the 35th International Conference on Machine Learning*, volume 80 of *Proceedings of Machine Learning Research*, pp. 5247–5256. PMLR, 10–15 Jul 2018. URL `https://proceedings.mlr.press/v80/weiss18a.html`.

Gail Weiss, Yoav Goldberg, and Eran Yahav. Learning deterministic weighted automata with queries and counterexamples. In H. Wallach, H. Larochelle, A. Beygelzimer, F. d'Alché-Buc, E. Fox, and R. Garnett (eds.), *Advances in Neural Information Processing Systems*, volume 32. Curran Associates, Inc., 2019. URL `https://proceedings.neurips.cc/paper_files/paper/2019/file/d3f93e7766e8e1b7ef66dfdd9a8be93b-Paper.pdf`.

R.J. Williams. Training recurrent networks using the extended kalman filter. In *[Proceedings 1992] IJCNN International Joint Conference on Neural Networks*, volume 4, pp. 241–246 vol.4, 1992. doi: 10.1109/IJCNN.1992.227335.

Y. Wu, L. Liu, J. Bae, K. Chow, A. Iyengar, C. Pu, W. Wei, L. Yu, and Q. Zhang. Demystifying learning rate policies for high accuracy training of deep neural networks. In *2019 IEEE International Conference on Big Data (Big Data)*, pp. 1971–1980, Los Alamitos, CA, USA, dec 2019. IEEE Computer Society. doi: 10.1109/BigData47090.2019.9006104. URL `https://doi.ieeecomputersociety.org/10.1109/BigData47090.2019.9006104`.

A Derivation

Lemma: The posterior probability $p(s_t|\tilde{z}_{1:t})$ is a monotonic function of the likelihood $p(\tilde{z}_t|s_t)$.

Proof:

$$\begin{aligned} p(s_t, \tilde{z}_{1:t}) &= p(s_t, \tilde{z}_t, \tilde{z}_{1:t-1}) && \text{The joint probability.} \\ &= p(\tilde{z}_t|s_t) \sum_{i=2}^{t} p(s_i|s_{i-1}) p(s_{i-1}, \tilde{z}_{1:i-1}) \\ &= C \cdot p(\tilde{z}_t|s_t) \\ &= \alpha_t(s_t) \end{aligned}$$

where we collect terms that do not depend on the likelihood into the constant C.

$$\begin{aligned} p(\tilde{z}_{1:t}) &= \sum_{i=1}^{t} \alpha_i(s_i) \\ &= \alpha_t(s_t) + \sum_{i=1}^{t-1} \alpha_i(s_i) \\ &= C \cdot p(\tilde{z}_t|s_t) + D \end{aligned}$$

where we collect new terms that do not depend on the likelihood into D. So:

$$\begin{aligned} p(s_t|\tilde{z}_{1:t}) &= \frac{p(s_t, \tilde{z}_{1:t})}{p(\tilde{z}_{1:t})} \\ &= \frac{C \cdot p(\tilde{z}_t|s_t)}{C \cdot p(\tilde{z}_t|s_t) + D} \end{aligned}$$

$\frac{\partial p(s_t|\tilde{z}_{1:t})}{\partial p(\tilde{z}_t|s_t)}$ is positive, so the posterior is monotonic with respect to the likelihood. □

Proposition 1 *We can rank features $\tilde{z}_t[i]$ according to how much they change the posterior probability $p(s_t = k|\tilde{z}_{1:t})$ by computing the derivative:*

$$\frac{\partial \log \mathcal{L}}{\partial \Delta \tilde{z}_t[i]} = \Sigma_k^{-1}[i, i]$$

It follows from monotonicity that if a unit perturbation in feature $\tilde{z}_t[i]$ results in the n-th largest change in the log probability $p(\tilde{z}_t|s_t = k)$, the perturbation also produces the n-th largest change in the posterior probability $p(s_t = k|\tilde{z}_{1:t})$. Therefore, we can simply rank features by their derivative w.r.t. the log likelihood.

Let $\Delta\tilde{z}_t[i]$ be a unit perturbation along feature i. In this work, we use Gaussian HMMs. The derivative of the log likelihood of a Gaussian is:

$$\begin{aligned} \frac{\partial \log p(\tilde{z}_t + \Delta\tilde{z}_t[i]|s_t = k)}{\Delta\tilde{z}_t[i]} &= \Sigma_k^{-1}(\tilde{z}_t + \Delta\tilde{z}_t[i] - \mu) \\ &= \Sigma_k^{-1}\Delta\tilde{z}_t[i] + E && E \text{ does not depend on } \Delta\tilde{z}_t[i]. \\ &= \Sigma_k^{-1}[i, i] && \Delta\tilde{z}_t[i] \text{ is a unit vector.} \end{aligned}$$

By the above, to rank features by $\frac{\partial \log p(\tilde{z}_t+\Delta\tilde{z}_t[i]|s_t=k)}{\Delta\tilde{z}_t[i]}$ is to rank features by their $\Sigma_k[i, i]^{-1}$, a value from the inverted covariance matrix. □

B Metrics

Name	Description
L_1	The L_1-norm, averaged over matrices. $\frac{1}{K}\|w\|_1 = \frac{1}{K}\sum_{i=1}^{n}\|w_i\|$, where K is the number of weight matrices in the neural network. We average over matrices so that models with different depths are comparable.
L_2	The L_2-norm, averaged over matrices. $\frac{1}{K}\|w\|_2 = \frac{1}{K}\sum_{i=1}^{n}\sqrt{w_i^2}$
$\frac{L_1}{L_2}$	Measures the sparsity of the weights. $\frac{1}{K}\sum_{i=1}^{K}\frac{L_1^{(i)}}{L_2^{(i)}}$, which is the metric $\frac{L_1}{L_2}$ averaged over the K weight matrices. Lower is more sparse. For example, a one-hot vector is fully sparse and has code sparsity of 1. See Hurley & Rickard (2008) for a discussion on measures of sparsity.
$\mu(w)$	Sample mean of weight. $\frac{1}{N}\sum_{i=1}^{N} w_i$, where N is the number of parameters in the network.
$median(w)$	Median of the weights, treated as a set concatenated together.
$\sigma(w)$	Sample variance of weights without Bessel's correction. $\frac{\sum_{i=1}^{N}(w_i-\bar{w})^2}{N}$
$\mu(b)$	Sample mean of the biases. We treat the biases separately because they have a distinct interpretation from the weights.
$median(b)$	Median of the biases, treated as a set concatenated together.
$\sigma(b)$	Sample variance of biases without Bessel's correction.
trace	The average trace over K weight matrices. $\frac{1}{K}\sum_{i=1}^{K}\texttt{tr}(W_k)$, where W_k is the kth weight matrix.
λ_{max}	The average spectral norm. $\frac{1}{K}\sum_{i=1}^{K}\|W_k\|_2$.
$\frac{trace}{\lambda_{max}}$	Average trace over spectral norm. $\frac{1}{K}\sum_{i=1}^{K}\frac{\texttt{tr}(W_k)}{\|W_k\|_2}$.
$\mu(\lambda)$	Average singular value over all matrices.
$\sigma(\lambda)$	Sample variance of singular values over all matrices.

Table 3: A glossary of metrics. The "Name" column is how the metrics appear in the text.

C Training Hyperparameters

For the MultiBERTs (Sellam et al., 2022), we use the open-source training checkpoints without any additional training.

Hyperparameter	Value
Learning Rate	1e-1
Batch Size	32
Training data size (randomly generated)	1000
Test data (randomly generated)	100
Architecture	Multilayer perceptron
Number of hidden layers	1
Model Hidden Size	128
Weight Decay	0.01
Seed	0 through 40
Optimizer	SGD

Table 4: Sparse parities, replicating Barak et al. (2022)

Hyperparameter	**Value**
Learning Rate	1e-3
Batch Size	2048
Training data size	3831 (30% of all possible samples)
Architecture	Transformer, no layer normalization
Transformer Number of Layers	1
Transformer Number of Heads	4
Model Hidden Size	128
Model Head Size	32
Weight Decay	1.0
Seed	0 through 40
Optimizer	AdamW

Table 5: Modular addition, replicating Nanda et al. (2023). To **stabilize** training (Figure 5), we reduced the batch size from 2048 to 256 and added back layer normalization.

Hyperparameter	**Value**
Learning Rate	1e-3
Batch Size	256
Training data size	50000 (splits downloaded from PyTorch)
Architecture	ResNet18
Weight Decay	1.0
Seed	0 through 40
Optimizer	AdamW
Data preprocessing	Random crop, random horizontal flip, and normalization

Table 6: CIFAR-100. To **destabilize** training (Figure 4), we removed batch normalization and residual connections.

Hyperparameter	**Value**
Learning Rate	1e-3
Batch Size	256
Training data size	60000 (splits downloaded from PyTorch)
Architecture	MLP
Number of hidden layers	1
Hidden size	800
Weight Decay	1.0
Seed	0 through 40
Optimizer	AdamW
Data preprocessing	Flatten to vector

Table 7: MNIST. MLP hyperparameters based on Simard et al. (2003).

D Language Modeling: MultiBERTs

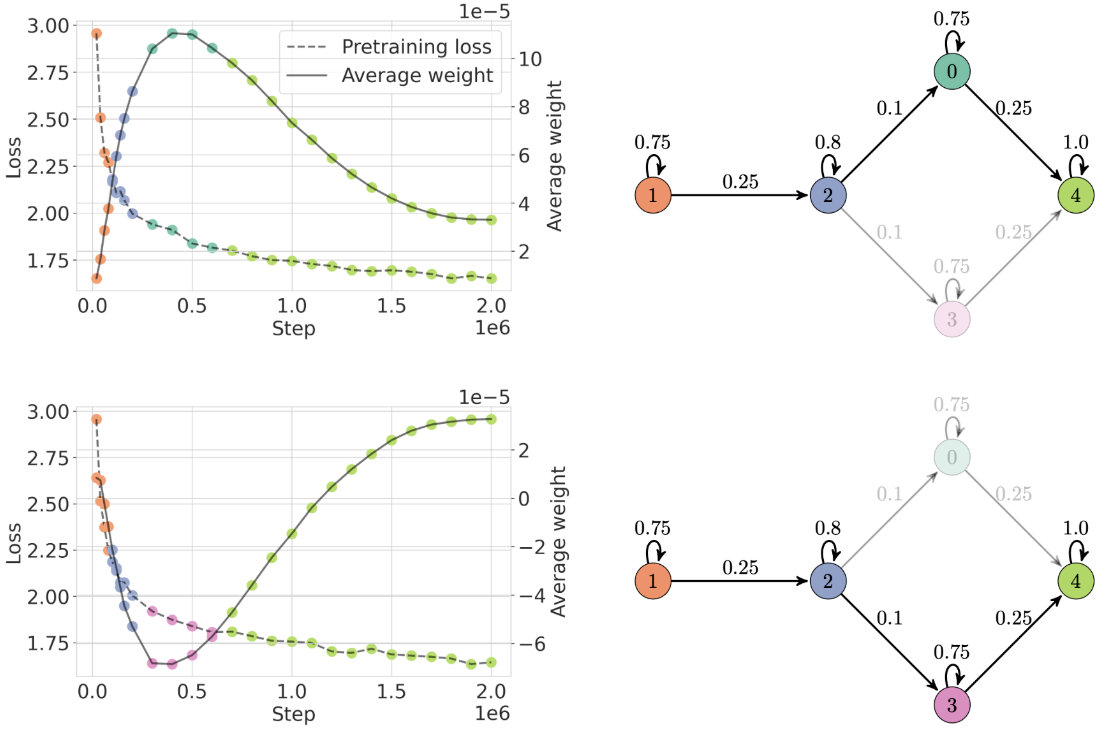

Edge	Top 3 important feature changes, by z-score	# of runs using edge (5 total)
2 → 0	median weight ↑1.69, average weight ↑1.70, max(λ) ↑1.14	2
2 → 3	median weight ↓1.33, average weight ↓1.30, max(λ) ↑1.11	3

Figure 7: MultiBERTs. The average weight $\frac{1}{N}\sum_i^N w_i$ initially decreases in two of the five MultiBERT runs (2 → 0) and increases in the other three (2 → 3). However, all runs eventually converge to roughly the same average weight. The HMM represents this difference in runs as the states 0 and 3. Critically, this difference is imperceptible from the pretraining loss.

To study variation in masked language model training, we use the five released training trajectories from the MultiBERTs (Sellam et al., 2022), which are replications of the original BERT model (Devlin et al., 2019), trained under different random seeds. MultiBERTs differs from the other settings we consider because its training occurs over the course of a single epoch, rather than over multiple epochs.

The most notable feature of the MultiBERTs training map is the fork at state 2. The average weights of the MultiBERTs models all converge to around 3.7×10^{-5}, but the paths that the five models take to get there can be clustered into two different trajectories. For the path including (2 → 0), the average weight increases during states 2 and zero and then decreases during state 4, while the opposite is true for paths including (2 → 3). Understanding this difference between MultiBERTs models could be a fruitful area for future work. Critically, this difference in model internals is imperceptible from the pretraining loss, which decreases at roughly the same rate for all five MultiBERTs runs. However, the MultiBERTs exhibit significant variation in transfer learning performance and gender bias Sellam et al. (2022), so these paths may indicate differences in behavior under specific distribution shifts and settings.

E Algorithmic Data: Sparse Parities

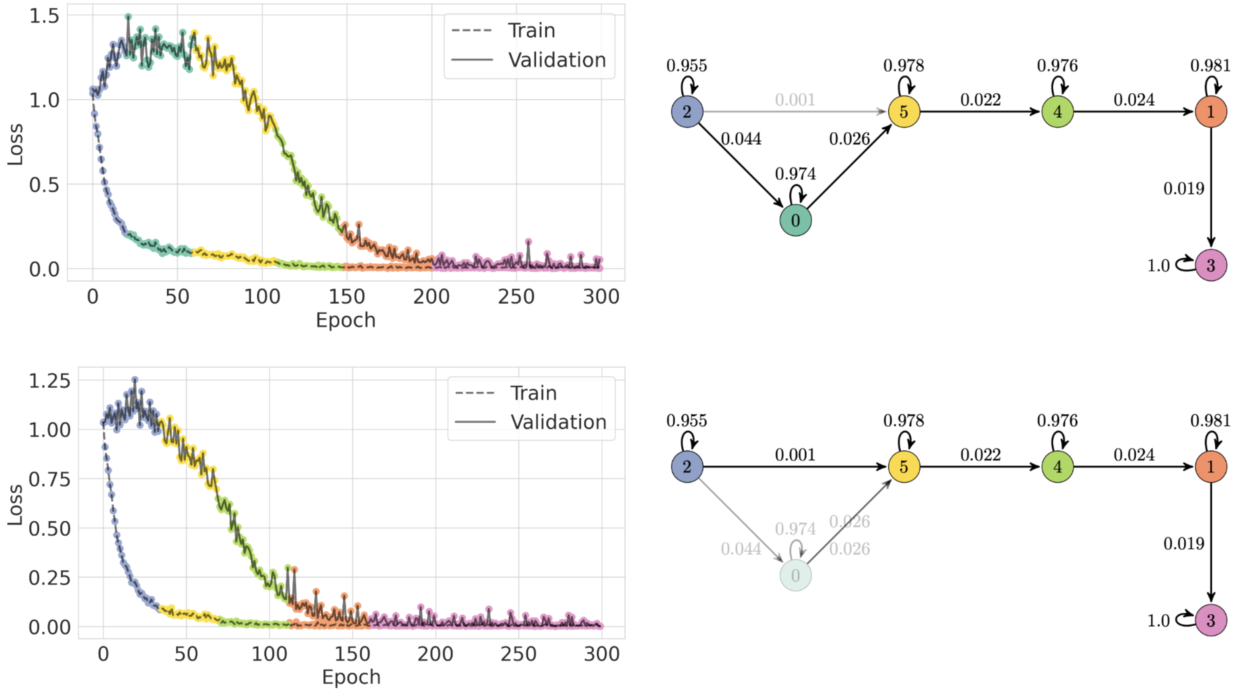

Edge	Top 3 important feature changes, by z-score	# of runs using edge (40 total)
$2 \rightarrow 0$	$L_2 \uparrow 0.11$, $L_1 \downarrow 0.61$, $\frac{L_1}{L_2} \downarrow 0.32$	39
$2 \rightarrow 5$	$L_2 \downarrow 0.19$, $L_1 \downarrow 1.01$, $\frac{L_1}{L_2} \downarrow 0.54$	1

Figure 8: Sparse parities. Faster generalization in sparse parities occurs with an early decrease in the L_2 norm. The norm ratio $\frac{L_1}{L_2}$ is a metric for dispersion, and it decreases as the vector becomes more sparse. For example, a one-hot vector is completely sparse and is the minimum of $\frac{L_1}{L_2}$.

F Image Classification: MNIST

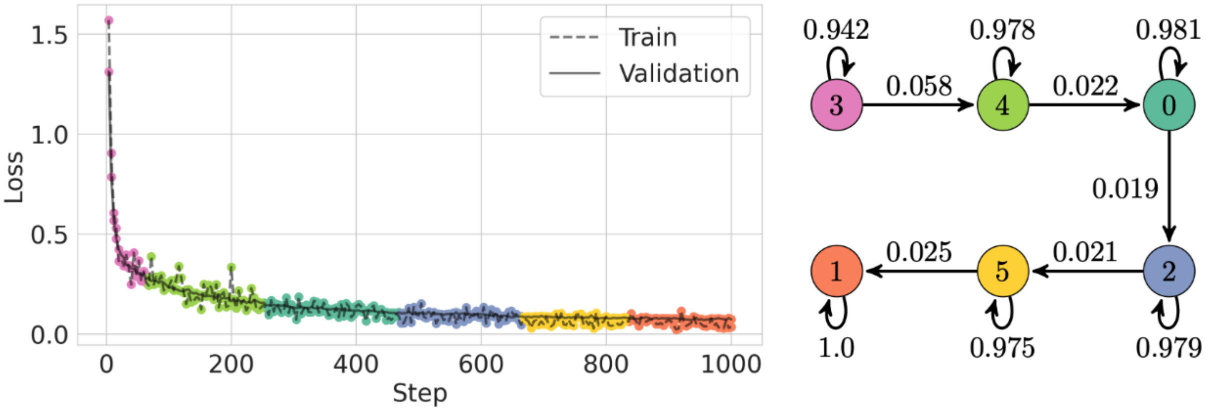

Edge	Top 3 important feature changes, by z-score
$3 \rightarrow 4$	$L_2 \uparrow 0.62$, $Var(w) \uparrow 0.58$, $L_1 \uparrow 0.61$
$0 \rightarrow 2$	$L_2 \uparrow 0.69$, $Var(w) \uparrow 0.70$, $L_1 \uparrow 0.70$
$5 \rightarrow 1$	$L_2 \uparrow 0.46$, $Var(w) \uparrow 0.50$, $L_1 \uparrow 0.48$

Figure 9: MNIST. All 40 training runs we collected from MNIST follow the same path, although individual runs can spend slightly different amounts of time in each state. As shown by the training map and accompanying annotations in the table, the training dynamics of MNIST are similar between states.

G Model Selection Curves

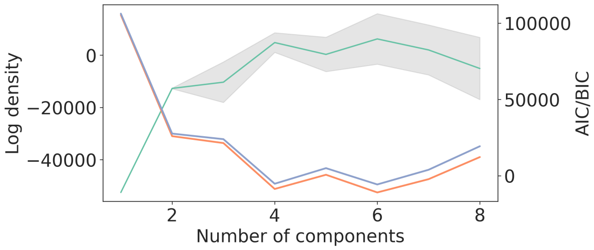

(a) Modular addition. 6 components.

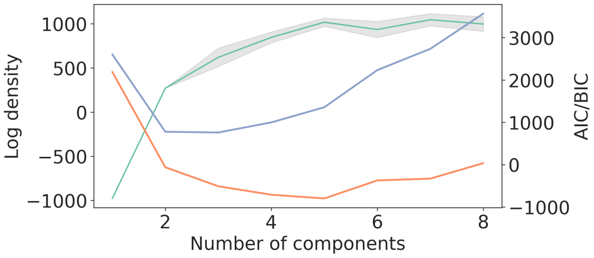

(b) Modular addition, stabilized. 3 components.

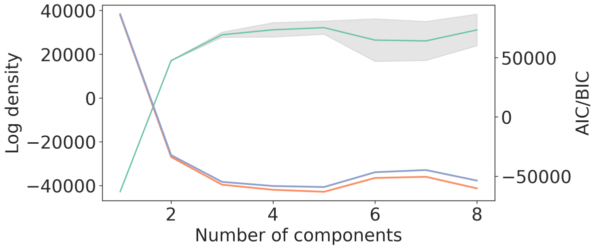

(c) CIFAR-100. 5 components.

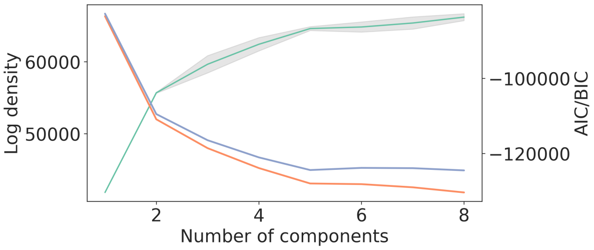

(d) CIFAR-100, destabilized. 5 components.

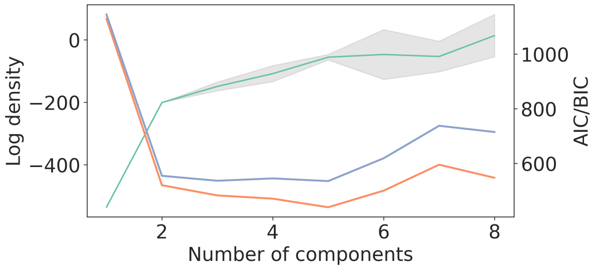

(e) MultiBERTs. 5 components.

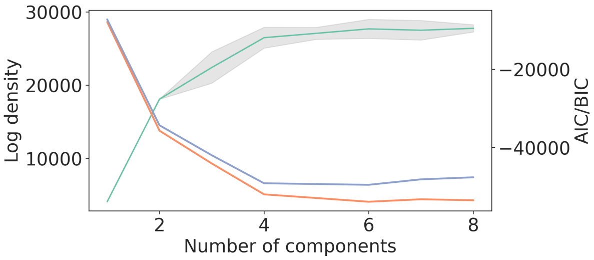

(f) Sparse parities. 6 components.

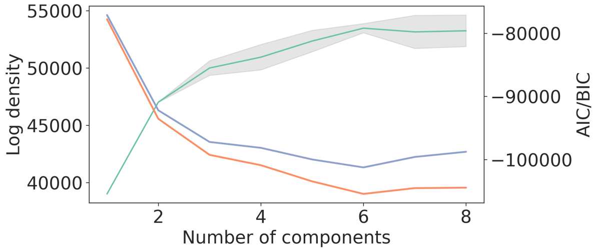

(g) MNIST. 6 components.

Figure 10: Model selection curves for choosing the number of hidden states in the HMM. We choose the model with minimum BIC in all cases.

H Convergence Time Histograms

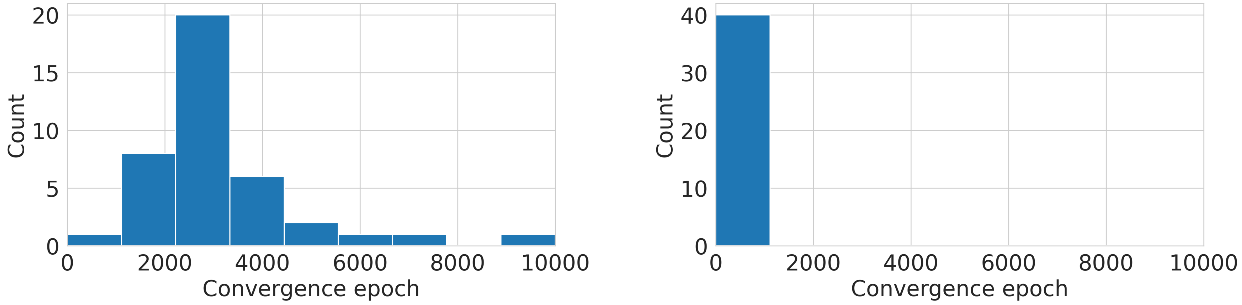

(a) Modular addition. Threshold 0.9.

(b) Modular addition, stabilized. Threshold 0.9.

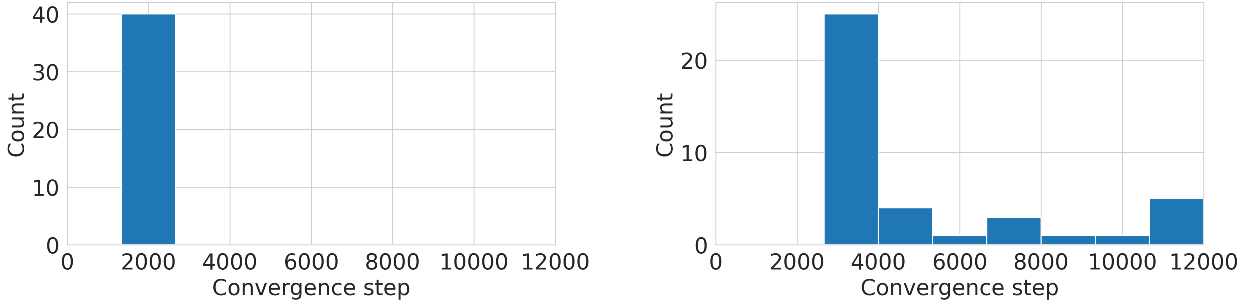

(c) CIFAR-100. Threshold: 0.6.

(d) CIFAR-100, destabilized. Threshold: 0.4.

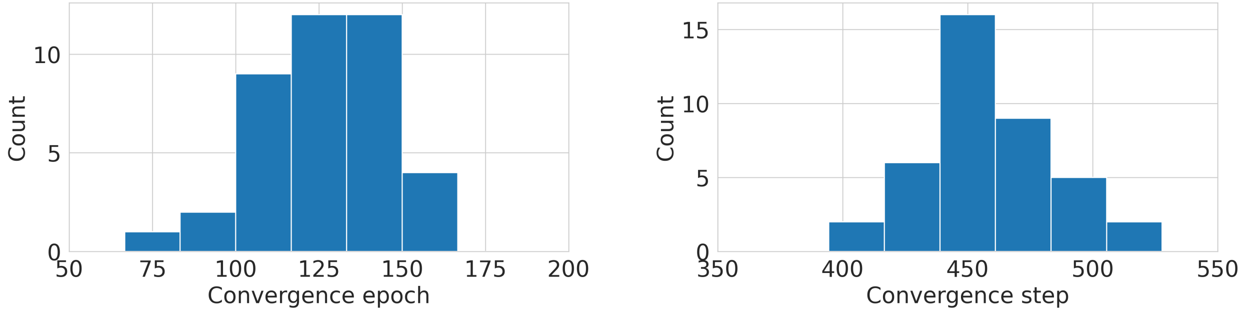

(e) Sparse parities. Threshold: 0.9.

(f) MNIST. Threshold: 0.97.

Figure 11: Visualization of convergence times. Convergence time here is defined as the first time a model crosses some threshold of evaluation accuracy, and choose the threshold to be a value slightly less than the performance that the final model achieves. For example, our fully trained models generally achieve perfect accuracy on modular addition, so we choose a threshold of 0.9.